

Diffusion and desorption of SiH₃ on hydrogenated H : Si(100) – (2 × 1) from first principles.

Michele Ceriotti* and Marco Bernasconi

*Dipartimento di Scienza dei Materiali and CNISM,
Università di Milano-Bicocca, Via R. Cozzi 53, I-20125, Milano, Italy*

We have studied diffusion pathways of a silyl radical adsorbed on the hydrogenated Si(100)-(2×1) surface within density-functional theory. The process is of interest for the growth of crystalline silicon by plasma-enhanced chemical vapor deposition (PECVD). Preliminary searches for migration mechanisms have been performed using metadynamics simulations. Local minima and transition states have been further refined by using the Nudged-Elastic-Band method. Barriers for diffusion from plausible adsorption sites as low as 0.35 eV have been found, but trap states have also been spotted, leading to a more stable configuration, with escape barriers of 0.80 eV. Diffusion through weakly bound physisorbed states is also possible with very low activation barriers (<50 meV). However, desorption mechanisms (either as SiH₃ or as SiH₄) from physisorbed or more strongly bound adsorption configurations turn out to have activation energies similar to diffusion barriers. Kinetic Monte Carlo simulations based on ab-initio activation energies show that the silyl radical diffuses at most by a few lattice spacing before desorbing at temperatures in the range 300-1000 K.

PACS numbers: 81.15.Gh 68.47.Fg 68.43.Bc

I. INTRODUCTION

Plasma-enhanced chemical vapor deposition (PECVD) from silane is a widespread technique employed to grow thin films of amorphous silicon.¹ High growth rates are made possible by the deposition of reactive radicals produced in the plasma, as opposed to conventional CVD where the less reactive silane is directly adsorbed at the growing surface. By suitably controlling the energy of the ions while keeping a high density of reactants, a related technique, called low-energy plasma-enhanced chemical vapor deposition (LEPECVD),^{2,3,4,5} has introduced the possibility to obtain device-quality epitaxial films of crystalline silicon or silicon-germanium alloys, at temperatures much lower (600 °C) than those necessary for conventional, thermal chemical vapor deposition (800 °C). SiH₃ is supposed to be the most abundant radical species in the plasma discharge in most of the experimental conditions^{6,7}. A description of the interactions of the silyl radical with the crystalline Si(100) surface is then of great interest to model the epitaxial growth at conditions of both PECVD and LEPECVD.

The silyl radical can interact with the surface giving rise to different processes: it can remove a hydrogen from a saturated dimer via an Eley-Rideal mechanism, or it might adsorb on the surface, where it would further evolve by diffusing, decomposing with hydrogen release at the surface or by desorbing (either as SiH₃ or SiH₄).

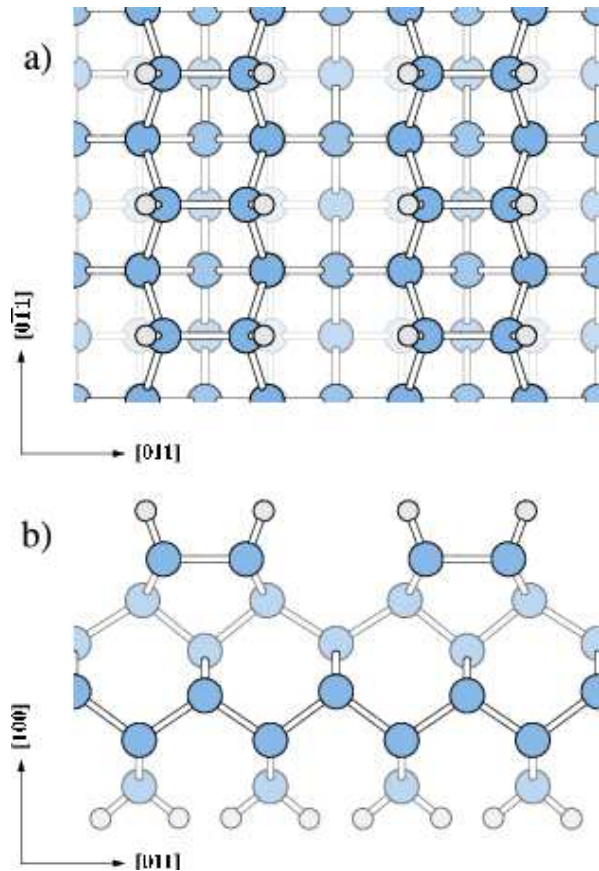
The fate of the silyl radical depends on the degree of surface hydrogenation at the landing site. At low hydrogen coverage the silyl can adsorb on a silicon dangling bond and decompose easily (into SiH₂ for instance⁸). The sticking probability is supposed to decrease at higher hydrogen coverage. The decomposition of the adsorbed radical is also supposed to be strongly hindered by the lack of free silicon surface atoms to which H might be transferred. Diffusion of the adsorbed silyl from hydro-

gen rich to hydrogen poor regions might be a conceivable route for SiH₃ decomposition and insertion into the growing film. Fast diffusion of SiH₃ adsorbed on the hydrogenated H:Si(100)-(2x1) surface has been recently predicted by first principles calculations^{9,10}. An equally fast diffusion of silyl radicals at the hydrogenated surface of amorphous silicon is also often invoked as the reason behind the high smoothness of the amorphous films grown by PECVD¹⁰. Although several processes involving the adsorbed silyl radical at the Si(100) surface have already been investigated in literature, previous theoretical studies always considered *a-priori* guess of reaction pathways, a procedure which might overlook unexplored mechanisms for diffusion and reaction of the adsorbed species.^{9,10,11,12,13,14,15,16}

In this paper, we investigate further the diffusion of SiH₃ adsorbed on the H:Si(100)-(2x1) surface by making use of the ab-initio metadynamics technique^{17,18}, a new simulation tool which allows for extensive search of diffusion pathways. Local minima visited during metadynamics trajectories have been then optimized and migration barriers between different minima further refined by the Nudged Elastic Band (NEB) method^{19,20}. Competitive mechanisms for diffusion and desorption have been investigated by Kinetic Monte Carlo simulations which provide the average diffusion length the silyl radical travels before eventually desorbing.

After a brief description of our theoretical framework in Section II, we present in Section III A our results on the diffusion mechanisms for the adsorbed silyl radical, on the existence of trap states which hinder the radical mobility and on desorption processes which compete with diffusion. In Section III we report the results of the Kinetic Monte Carlo simulations based on the ab-initio activation energies which has allowed estimating the effect of possible errors in the calculated activated energies on the fate of the silyl radical. Sec. IV is devoted to our

FIG. 1: (color online) The slab model of the H : Si(100) – (2 × 1) surface, from a top a) and side b) views.



conclusions.

II. COMPUTATIONAL DETAILS

Calculations have been performed within the framework of Density Functional Theory (DFT) with a gradient corrected exchange and correlation energy functional (PBE)²¹ as implemented in the codes PWSCF²² for geometry optimizations and NEB¹⁹ calculations and CPMD²³ for Car-Parrinello²⁴ metadynamics simulations^{17,18}. Norm-conserving²⁵ and ultrasoft²⁶ pseudopotentials have been used for silicon and hydrogen, respectively. Kohn-Sham orbitals are expanded in plane waves up to kinetic energy cutoff of 25 Ry. Selected calculations have been repeated with a norm conserving pseudopotential for H as well and a kinetic cutoff of 30 Ry.

As preliminary tests of our framework, we have calculated the reaction enthalpies for some decomposition reactions of disilane (Si_2H_6) within a cubic supercell of edge 15.3 Å. Both PBE and BLYP^{27,28} have been used for these benchmark calculations on molecular systems. Geometries have been optimized until the maximum resid-

TABLE I: Reaction energies (ΔU_0) and enthalpies (ΔH , in eV) calculated for some gas-phase decomposition reactions of disilane. Results obtained with PBE and BLYP functionals are compared to experimental data and previous quantum-chemical results.

$\text{Si}_2\text{H}_6 \rightarrow$	$\text{SiH}_2 + \text{SiH}_4$	$\text{H}_2 + \text{Si}_2\text{H}_4$	$\text{SiH}_3 + \text{SiH}_3$
ΔU_0 PBE	2.559	2.169	3.147
ΔU_0 PBE ^a			4.158
ΔU_0 BLYP	2.213	2.099	2.984
ΔU_0 MP2 ^b	2.436	2.375	3.182
ΔH PBE	2.445	2.033	3.028
ΔH BLYP ^c	2.098	1.963	2.865
ΔH MP2 ^b	2.355	2.064	3.048
ΔH B3LYP ^d	2.259	2.025	3.265
ΔH Exp. ^d	2.355	2.021	3.326

^aSpin restricted calculation

^bMP2/6-311++g** results from Ref.³⁶

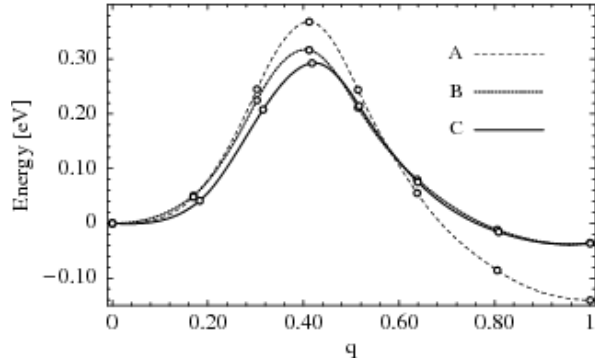
^cVibrational contributions to enthalpy from PBE normal modes.

^dfrom Ref.³⁷

ual force on every atom was less than 0.01 eV/Å. Formation enthalpies have been calculated taking into account the vibrational contribution to the quantum partition function in the harmonic regime, with normal modes obtained, in turn, by diagonalization of the dynamical matrix, built from the numerical derivatives of the forces with respect to finite atomic displacements (0.015 Å). Rotational and translational contributions to reaction enthalpies have been added in the classical limit. Results for PBE and BLYP functionals are compared in Table I with experimental data and previous quantum-chemical calculations. The results are in good agreement with experiments and higher levels of theory, PBE performing overall better than BLYP functional. For reactions involving homolytic bond breaking such as the decomposition $\text{Si}_2\text{H}_6 \rightarrow 2\text{SiH}_3$, spin unrestricted calculations allowing spin polarization are mandatory to reproduce the correct reaction enthalpies. Neglect of spin polarization (spin restricted calculations) introduces errors as large as 1 eV (cf. Table I) in the reaction energies. All the surface calculations have been then performed in a spin unrestricted framework (LSD-PBE).

The H:Si(001)(2x1) surface is modeled in a slab geometry with 3D periodic boundary conditions (see Fig.1). The theoretical equilibrium lattice parameter obtained from a bulk calculation with the k-point sampling corresponding to the supercell Γ -point is 0.7 % larger than the experimental one, while the theoretical value at full convergence in BZ integration is 0.6 % shorter than the experimental one. Thus, in the slab calculation we chose the experimental lattice parameter (5.43 Å²⁹) as an average value of the theoretically lattice constants that can be obtained with different supercell sizes and k-point sampling. In a previous work³⁰, we checked that by changing the lattice parameter by 0.7 %, the adsorption energy of the silyl radical on the clean Si(001)-(2x1) surface changes by less than 10 meV. The periodically repeated

FIG. 2: Minimum energy path obtained by NEB optimization for the migration from the minimum (a) to the minimum (b) of Figure 4. The energy profile with respect to a suitably defined reaction coordinate q is reported. Path A is optimized with the Γ -point only. Path B corresponds to the total energies obtained with one special k -point in the surface BZ for the geometries of path A. Path C has been fully optimized by using one special k -point.



slabs are separated by vacuum, 11 Å wide. The slab has six silicon layers, each containing 12 atoms. The hydrogenated top surface, reconstructed in the (2x1) geometry, contains six hydrogenated silicon dimers. The bottom surface of the slab is saturated by symmetric SiH₂ groups. The SiH₂ groups and the underlying silicon layer were kept fixed at the ideal bulk positions. Only the supercell Γ -point has been considered in Brillouin Zone sampling for geometry optimizations. We checked the convergence of our results with respect to Brillouin Zone integration by optimizing selected geometries with the special k -point ($\frac{1}{4}, \frac{1}{4}$) (in crystallographic coordinates³¹). Calculations with large surface supercell (three rows of five dimers each) have also been performed for selected systems.

To uncover possible diffusion pathways of the silyl radical, we have made use of the metadynamics technique which allows large barriers to be overcome in an affordable simulation time (few picoseconds) within ab-initio molecular dynamics simulations.^{17,18} The method is based on a coarse-grained, non-Markovian dynamics in the manifold spanned by few reaction coordinates biased by a history-dependent potential which drives the system towards the lowest saddle point. The main assumption is that the reaction path could be described on the manifold of few collective variables (CV) $S_\alpha(\{\mathbf{R}_I\})$, function of the ionic coordinates \mathbf{R}_I . The Lagrangian \mathcal{L}_0 of the system is then modified, introducing an history-dependent biasing potential, which affects the dynamics so as to discourage the system from remaining in the region already visited and pushes it over the lowest energy barrier towards a new equilibrium basin. Many variations over these basic principles have been explored; in this paper we use the straightforward approach of Ref.³², which simply introduces a repulsive potential ($\mathcal{L} = \mathcal{L}_0 - g(\{\mathbf{R}_I\}, t)$) built from the superposition of Gaussians centered at points

previously visited by the trajectory in CV space, which acts directly on the ionic coordinates \mathbf{R}_I as

$$g(\{\mathbf{R}_I\}, t) = w \sum_{t_j < t} \exp \left[-\frac{\sum_{\alpha=1}^n (S_\alpha(\{\mathbf{R}_I(t)\}) - S_\alpha(\{\mathbf{R}_I(t_j)\}))^2}{2\Delta s^2} \right] \quad (1)$$

To study the diffusion of the adsorbed silyl radical, we have chosen as collective variables the (x, y) surface position of the silyl silicon atom (two CVs). The Gaussian hills parameters (Eq. 1) have been chosen as $\Delta s = 0.32$ a.u. and $w = 0.11$ eV; a new hill is added each time the trajectory reaches a point $2\Delta s$ far from the previous Gaussian in CV space, or at worst every 250 time steps. We have performed Car-Parrinello metadynamics simulations with a time-step of 6 a.u., effective mass for electrons of 600 a.u., and deuterium mass for hydrogen. Constant temperature (300 K) on ions is enforced by a Nosè-Hoover thermostat.³³

Although metadynamics allows computing activation free-energies from a finite temperature simulation, long simulation time (with small Gaussian height w) are needed to obtain accurate estimates of activation free energies. Actually, our metadynamics simulations are aimed at just obtaining a good starting guess for the transformation path. Then, the geometry and activation energy of the transition state identified along the dynamical trajectory have been further refined by using a standard technique with fixed end points, the Nudged Elastic Band (NEB) method.¹⁹ Climbing image and variable springs²⁰ have been used thoroughly (but for processes with a barrier below 0.10 eV, where a constant spring constant of 0.6 a.u. has been used), with spring constants $k_{max} = 0.6$ a.u. and $k_{min} = 0.3$ a.u.. A minimization scheme has been applied until the residual total forces acting on each image in direction perpendicular to the path was less than 0.05 eV. We have relaxed the Minimum Energy Path (MEP) using Γ -only calculations, then we have performed a self-consistent electronic structure optimization along the MEP using one special k -point. Full optimization of the MEP geometry with one special point (cf. Fig. 2 for a selected process) introduces changes in the activation energies of the order of a few tens of meV with respect to the calculation with one special point on the gamma-point geometry.

To obtain some figures describing qualitatively the behavior of the radical, and to test how much the fate of the radical is affected by variations of the calculated activation energies within the uncertainties of DFT (up to 0.1 eV). we have performed Kinetic Monte Carlo (KMC)³⁴ simulation based on the reaction scheme from metadynamics and NEB calculations.

KMC is a simulation technique which permits to attain large length and time scales, relying on the knowledge of the rates for all the relevant reaction mechanisms between local minima. The dynamics is performed stepwise, choosing at every step one of the possible mechanism with a probability proportional to its rate, and in-

crementing the simulation time by the appropriate time step following the scheme of Ref.³⁴.

III. RESULTS

A. Mechanisms for diffusion and desorption

The starting geometry of our metadynamics simulations corresponds to a SiH_3 radical adsorbed in the configuration of Fig. 4(a) previously identified as a possible adsorption geometry from first principles static calculations¹⁰ and from direct simulations of the impact of the silyl on the $\text{H:Si}(100)2\times 1$ surface³⁰. In fact, we have shown by targeted ab-initio MD simulations that the SiH_3 sticks on the surface in the configuration of Fig. 4(a) once it impinges on this site with a translational kinetic energy in the range 0.1-0.2 eV.³⁰

In a metadynamics run 10 ps long, we have observed the diffusion of the SiH_3 radical via configurations not previously considered in literature such as those sketched in Figure 3. Indeed, inspection on the molecular dynamics trajectories has allowed identifying several possible local minima and migration paths for the silyl radical which we have then refined by geometry optimization and NEB calculations as described below.

Sketches of the local minima resulting from geometry optimization of the metadynamics snapshots are shown in Fig. 4 (in the following, we will refer to “configuration (x)” as “the configuration sketched in Figure 4 (x)”) along with pictures of other structures taken from literature, or guessed by analogy with those identified in the metadynamics simulation. The energy of such minima are reported in Table II. As anticipated in section II we have checked the convergence of our results with respect to the size of the supercell and to the k-points sampling of the Brillouin Zone (BZ). Tests with more than one special k -point have revealed minute changes in energy differences (the desorption energy from the (a) site changes from 0.147 eV to 0.154 eV by using one or four special k -points in the total energy calculation on geometries optimized with Γ -point only). On the other hand, to achieve reasonable accuracy in activation energies, it is sufficient to use one special point on geometries optimized with gamma-point only (cf. Figure 2).

The calculated activation energies for the various migration processes among the different local minima are listed in Table III, and a schematic (and crowded) summary of the mechanisms examined is drawn in Figure 6.

Large disagreement is found for the adsorption energy with respect to some ab-initio results previously reported in literature. For instance in Ref.⁹ an adsorption energy of 0.63 and 0.75 eV are reported for silyl in configurations (a) and (g), while we obtain the values 0.15 and 0.35 eV, respectively. Similarly, the energy gain for the removal of a hydrogen by a silyl radical is as high as 0.86 eV in Ref.¹² to be compared with our result of 0.35 eV. A possible source of discrepancy might be the use of a

FIG. 3: (color online) Four snapshots from the metadynamics trajectory of silyl diffusion on $\text{H:Si}(100)-(2\times 1)$: a) $t = 0$ ps, b) $t = 2.1$ ps, c) $t = 3.5$ ps, d) $t = 10$ ps.

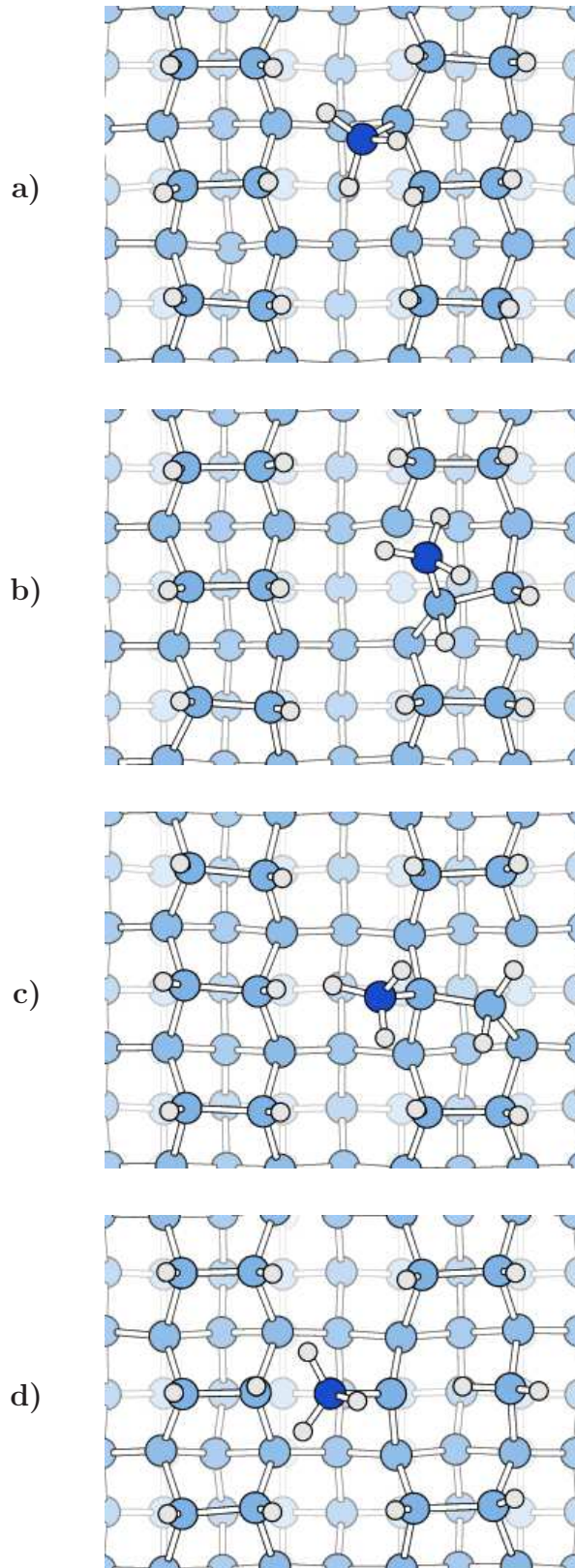


FIG. 4: (color online) Sketches of ten different local minima for SiH_3 adsorbed on $\text{H} : \text{Si}(100) - (2 \times 1)$ surface. Side views of (a) and (i) structures are also reported at the bottom to illustrate the difference in geometry between strongly bound and physisorbed minima. The structures (e) and (g) are not perfectly symmetric with respect to the dimer plane, so that two corresponding mirror structures exist; this small asymmetry is due to the balance between the interaction of the SiH_3 hydrogen atoms with the surface hydrides, and the barrier for interconversion between the mirror configurations is likely to be very low. For what concerns diffusion, the two mirror images can be regarded as a single, symmetric structure.

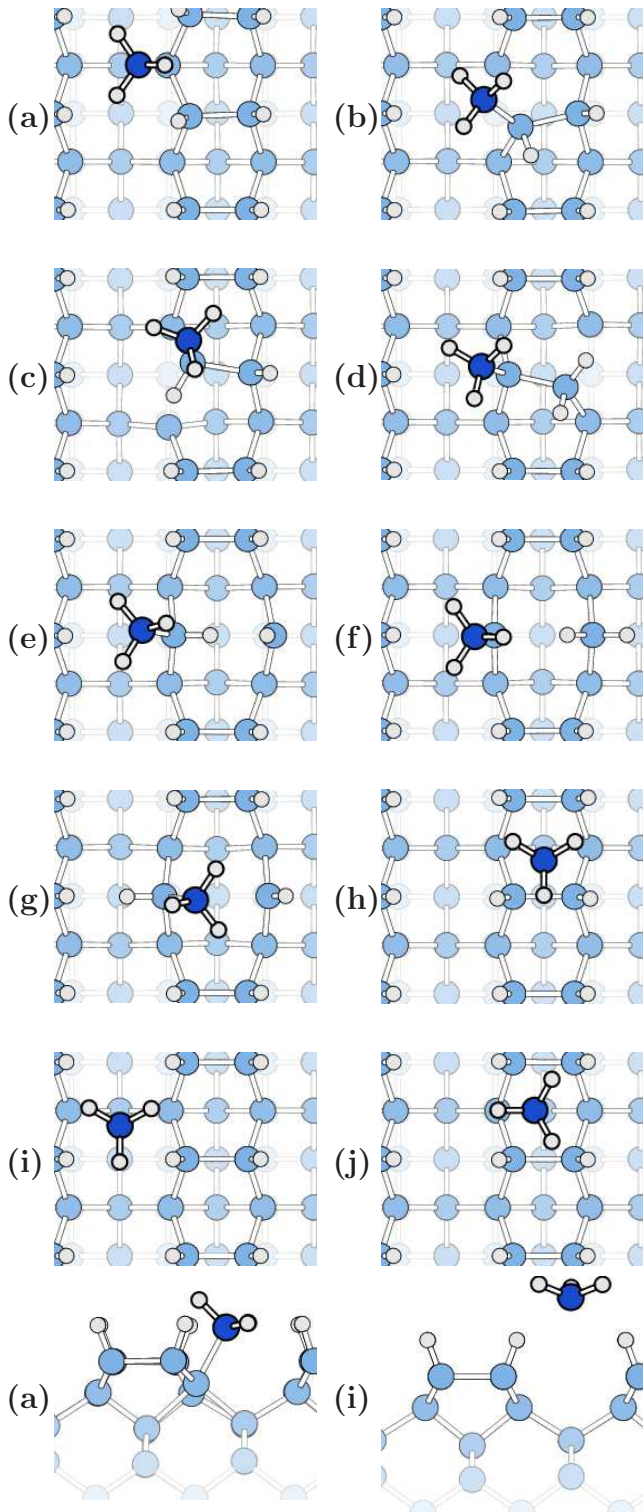


TABLE II: Energies (eV) of the local minima shown in Figure 4. The zero of energy corresponds to SiH_3 far from the surface, as computed from free surface and isolated silyl within the same supercell used to model the adsorbed silyl. $\text{SiH}_4 + db$ indicates the reaction energy of silane formation from a silyl radical abstracting a surface hydrogen atom. Column **A** refers to the results that are used throughout the paper, while other columns refer to various tests we performed on selected structures by changing k -points sampling and supercell size. Namely, column **A** refers to calculations with 6 dimers supercell and energies computed with one special k -point on geometries optimized with the Γ point only. Column **B** refers to the same calculations as in **A** with energies as well as geometries computed with the Γ point only. Column **C** refers to calculations with 6 dimers supercell with energies and geometries optimized with one special k -point. Column **D** refers to calculations with a 15 dimers supercell, energies and geometries optimized with Γ point only. Column **E** refers to calculations as in column **B** but without spin polarization, i.e. within a spin-restricted framework (LDA-PBE instead of LSD-PBE).

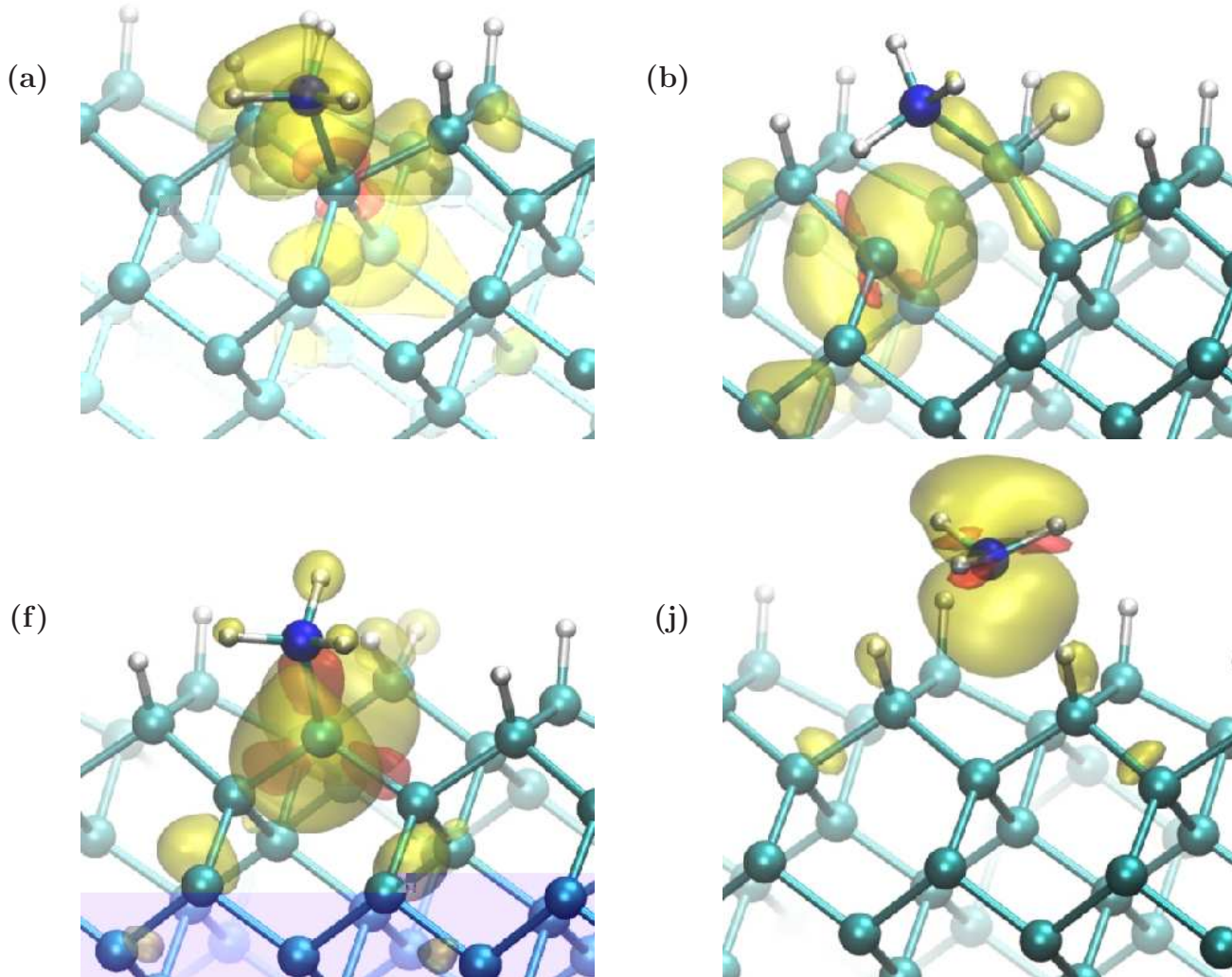
	A	B	C	D	E
a)	-0.15	-0.23	-0.14	-0.16	-0.64
b)	-0.18	-0.38		-0.23	
c)	-0.15	-0.32		-0.20	
d)	-0.25	-0.45	-0.26	-0.30	
e)	-0.34	-0.43		-0.36	
f)	-0.60	-0.67		-0.61	
g)	-0.37	-0.54			-0.64
h)	-0.06	-0.07			
i)	-0.04	-0.05			
j)	-0.07	-0.08			
SiH_3	0.00	0.00	0.00	0.00	0.00
$\text{SiH}_4 + db$	-0.50	-0.52	-0.50		-0.80

spin restricted framework in Ref.^{9,12}. Indeed, by repeating our calculation with no spin polarization we have obtained adsorption and reaction energies similar to those reported in previous works (column **E** in Table II). As discussed in Sec II, spin unrestricted framework is, however, recommended to properly describe an open shell system like the silyl radical, especially in the gas phase.

Except for the overcoordinated configuration (a), the local minima can be classified into three categories: configurations with a broken dimer ((e), (f), (g)), and the unpaired electron mostly localized on a surface Si atom, configurations with a broken backbone ((b), (c), (d)), and the unpaired electron localized onto a subsurface atom (see Figure 5), and finally weakly bound “physisorbed” configurations of the silyl radical ((h), (i), (j)). Configurations in the first category appear to be lower in energy than those in the second one, because the substrate is less strained and the $\text{H} - \text{H}$ repulsion is lower.

Configurations with adsorption energies in the range 0.15-0.35 eV are referred to hereafter as strongly bound adsorption states, while traps are states with still higher adsorption energies. The three “physisorbed” states could be reached from the gas phase with no activa-

FIG. 5: (color online) Spin polarization ($m(\mathbf{r}) = \rho_{\uparrow}(\mathbf{r}) - \rho_{\downarrow}(\mathbf{r})$) for the four configurations (a), (b), (f) and (j) of Figure 4, is shown in the four corresponding panels. Isosurfaces at $m = \pm 10^{-3}$ a.u. are reported, with colors depending on the spin sign. In the three structures, $\int d^3\mathbf{r} |m(\mathbf{r})|$ is approximately 1.2 au, corresponding to the unpaired electron introduced by the silyl, plus some polarization effects. Structure (a) shows the most pronounced spin delocalization, with the unpaired electron shared between the silyl silicon and two surface silicon atoms.



tion barrier. However, because of the very tiny adsorption energy, adsorption at these sites might have a low cross section. Indeed, these states have not been observed in our previous MD simulations of SiH_3 impinging on the surface with energy in the range 0.1-0.2 eV³⁰. The existence of a precursor state for silyl adsorption on hydrogenated surfaces has been proposed in early models of PECVD growth³⁵, although by assuming a physisorption geometry involving a three centers configuration ($\text{H}_3\text{Si} - \text{H} - \text{Si}_{\text{surf}}$) which has been ruled out by later *ab-initio* calculations on $\text{H} : \text{Si}(111)$ ¹¹ and $\text{H} : \text{Si}(100) 2 \times 1$ ³⁰ surfaces. The silyl can move from physisorbed states to configurations with a higher adsorption energy by overcoming tiny barriers (< 0.05 eV) which can be ascribed to hydride-hydride electrostatic repulsion.

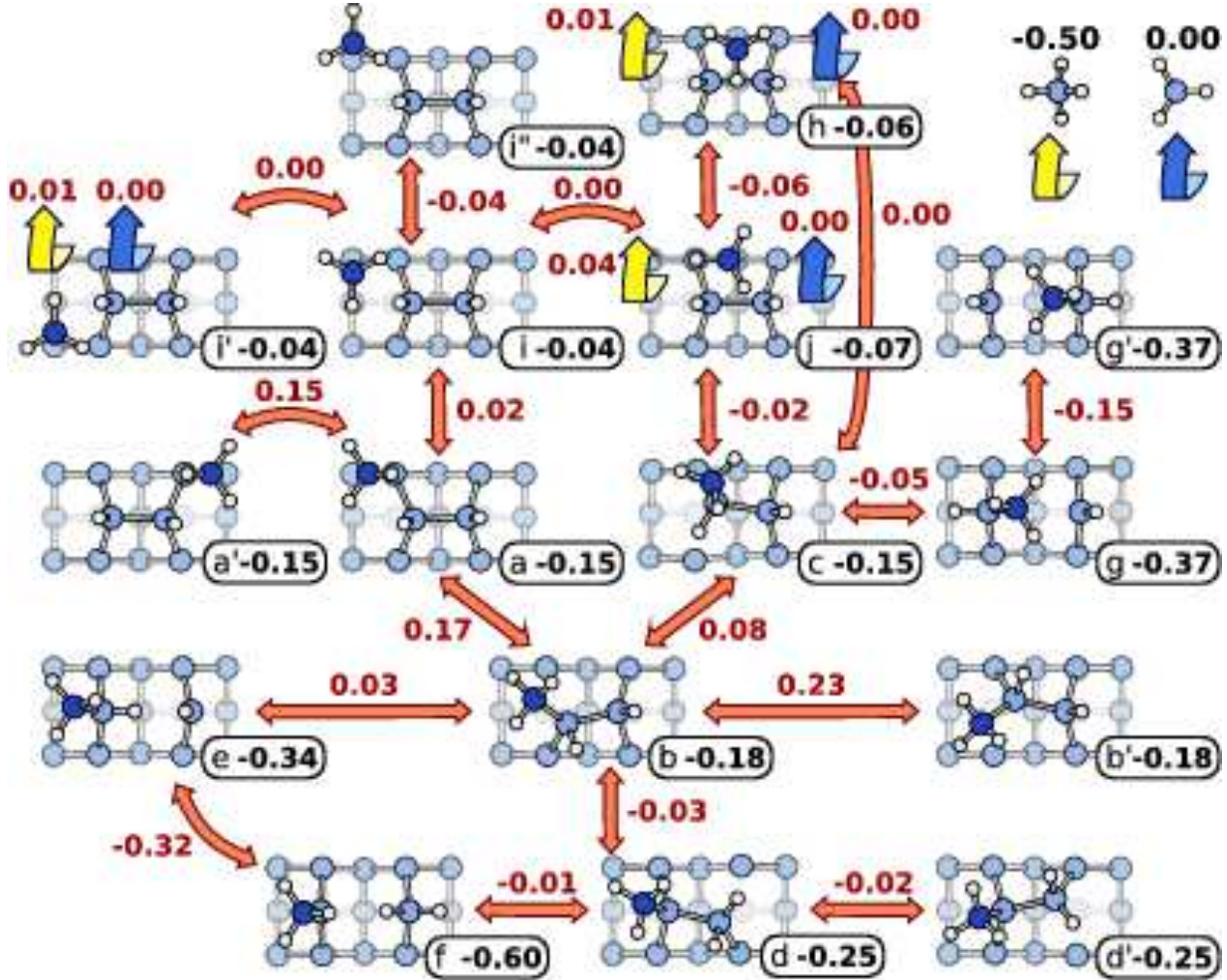
To complete the analysis of the adsorbed silyl, we have

also considered desorption processes, either as SiH_3 or as SiH_4 , with the concurrent removal of a surface hydrogen. We have not been able to obtain a direct desorption mechanism from the strongly bound adsorption states, as paths optimized with the NEB method always show the physisorbed states as intermediates. Desorption as silyl from physisorbed configurations (h), (i) and (j) takes place with no barrier other than the binding energy of the free radical. Energy barriers of 0.07, 0.05 and 0.11 eV have to be overcome by the silyl radical to leave the surface as a silane molecule by removing a nearby hydrogen from configurations (h), (i) and (j), respectively.

To simplify the discussion of Figure 6 which reports all the migration events we have investigated, at first let us consider jumps among strongly bound states.

Starting from configuration (a), we can identify two diffusion pathways, one parallel to the dimer rows (Fig-

FIG. 6: (color online) A synoptic scheme of the different migration mechanisms we have considered. The energy of local minima and transition states (in eV) are reported with reference to the desorbed SiH_3 (zero of energy). Activation energies for jumps in both directions can be obtained as energy differences. Transition-state energies for desorption from the physisorbed states, either as silyl or as silane, are also reported (large arrows).



ure 7 (a)) and the other in the perpendicular direction (Figure 7b). The overall activation barrier is 0.36 eV in both cases, corresponding to the key-event (b) \rightarrow (a). The direct (b) \rightarrow (b') conversion has a higher barrier than a mechanism which takes place via reversible hydrogen exchange between the dimer atoms ((b) \rightarrow (d) \rightarrow (d') \rightarrow (b')), which was spotted by metadynamics.

However, from configuration (b), the radical can reach the more stable state (f) state, following one of the two paths highlighted in Figure 8, both of which have activation energies lower than the activation barrier for diffusion. The deepest local minimum (f) acts as a “trap” state which hinders diffusion. The overall activation energy for diffusion from (f) site to an equivalent (f') site along the dimer row is as high as 0.77 eV. Even though the presence of the trap state rules out fast diffusion at low temperatures, a barrier of 0.7 eV is still sufficiently low to be easily overcome at room or growth temperatures. Still, we have not yet included the ph-

ysisorbed states into the picture. Actually, some diffusion pathways involving physisorbed states as intermediates have slightly lower barriers than the mechanisms involving strongly bound states only, e.g. the (a) \rightarrow (a') path shown in Figure 9 with an overall barrier of 0.17 eV.

The evolution of the adsorbed SiH_3 radical we have discussed so far can be summarized by the simplified scheme of Figure 10. A high barrier has to be overcome to escape from the realm of trap states and reach some “mobile” local minima. From one of those states, with similar barriers, the system might fall back into the traps, diffuse to nearby strongly bound states or reach one of the physisorbed states. Barriers for migration between different strongly bound states (~ 0.3 eV) are similar to barriers for migration between strongly bound and physisorbed states. From the latter physisorbed states, with barriers below 0.1 eV, the silyl can go back to the strongly bound states, diffuse amongst the physisorbed states or desorb, with similar barriers, either as silyl or as silane. The

FIG. 7: (color online) Diffusion pathways for a SiH_3 radical, a) parallel to the dimer row, and b) perpendicular to the dimer row. Energies of transition states and intermediate minima (in eV) are given. The zero of energy corresponds to the desorbed SiH_3 .

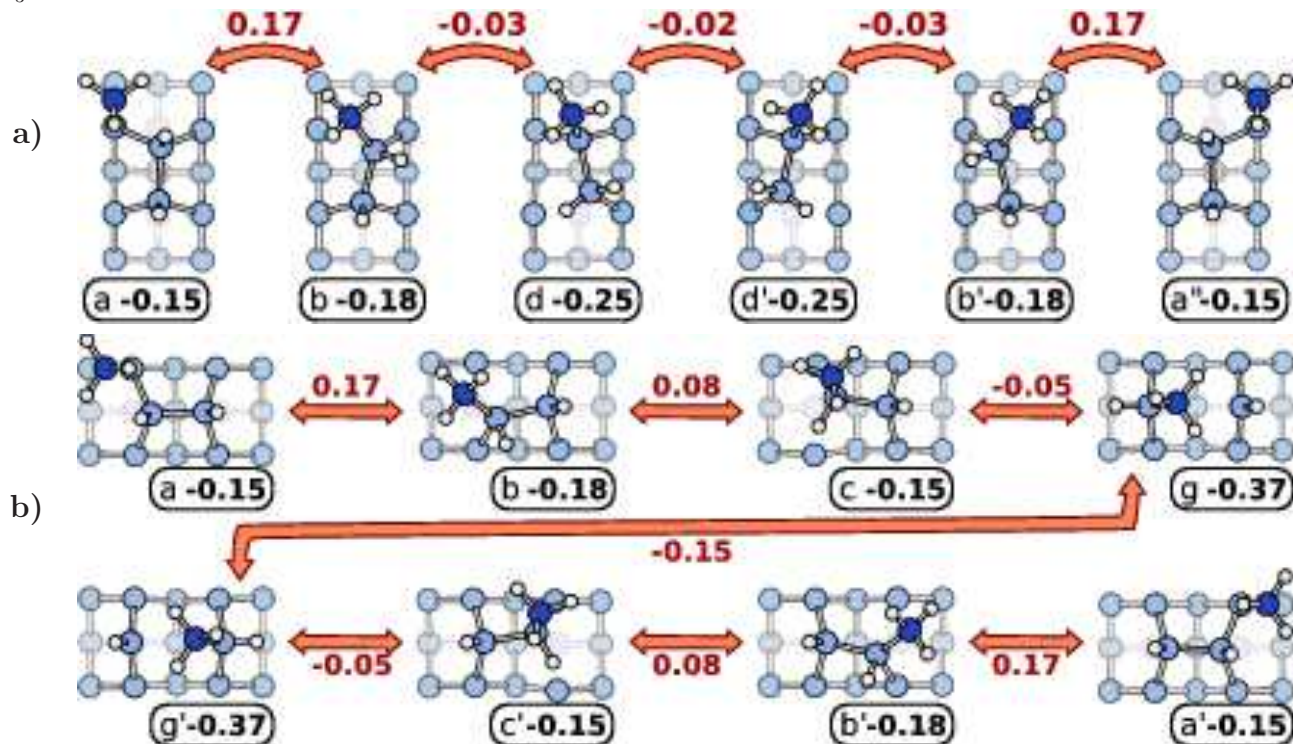
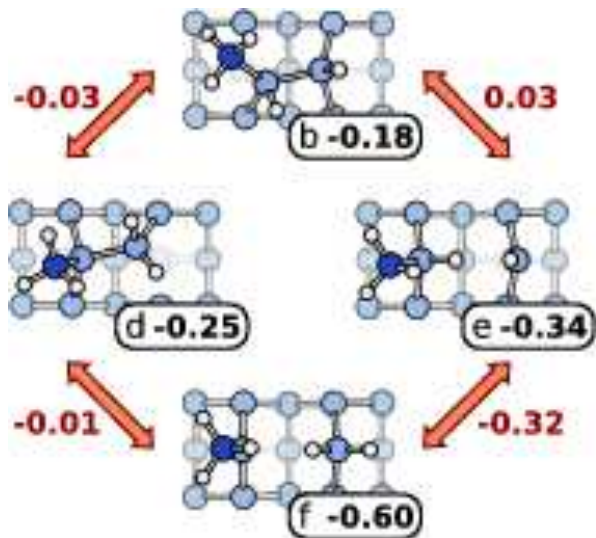
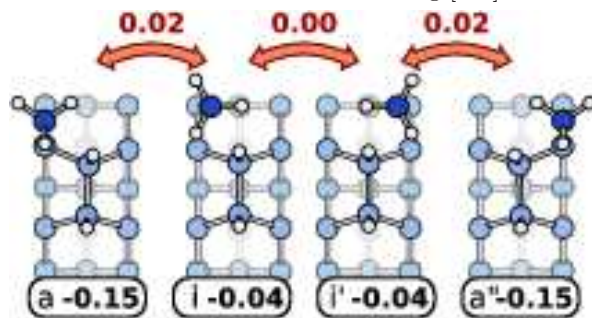


FIG. 8: (color online) Two paths leading to the trap state (f) from the local minimum (b). The zero of energy (eV) corresponds to the desorbed SiH_3 .



accuracy of our calculations is not sufficient to identify which are the dominant processes at low temperature, since uncertainties of the order of 0.1 eV in the activation energies are expected due to approximations in the exchange and correlation functional. However, at typi-

FIG. 9: (color online) A path for diffusion between two equivalent (a) sites, passing through physisorbed state (i). Energies (eV) of minima and transition states are given. The zero of energy corresponds to the desorbed SiH_3 . See Figure 4 for sketches of the two structures viewed along $[0\bar{1}1]$.



cal growth temperatures of PECVD and LEPECVD the different events are likely to have similar probability. To estimate the average diffusion length that a silyl radical can travel before desorption takes place, we have performed kinetic Monte Carlo simulations using the activation energies for the different processes summarized in Table III. The results are discussed in the next section.

As a final remark, we compare our results on diffusion mechanisms with previous ab-initio works appeared in literature. The migration (a) \rightarrow (a') between two adjacent dimers rows and the (g) \rightarrow (g') jump within an open

TABLE III: Activation energies (in eV) for various migration mechanisms of SiH_3 on $\text{H}:\text{Si}(100) - (2 \times 1)$. Column **B** reports values obtained by NEB optimization of the minimum energy path by sampling the BZ at the Γ -point only. Column **A** corresponds to the activation energies computed with one special k-point on geometries optimized with Γ -point only. The primed and not-primed configurations are equivalent by symmetry: (a) \rightarrow (a') corresponds to a jump across the channel, (b) \rightarrow (b') and (d) \rightarrow (d') corresponds to the conversion between two structures equivalent with respect to the mirror plane orthogonal to $[0\bar{1}1]$, (g) \rightarrow (g') corresponds to the migration of the radical between the two atoms of the broken dimer, (i) \rightarrow (i') and (i) \rightarrow (i'') correspond to two steps of a jump along the dimer row, between two equivalent physisorbed states.

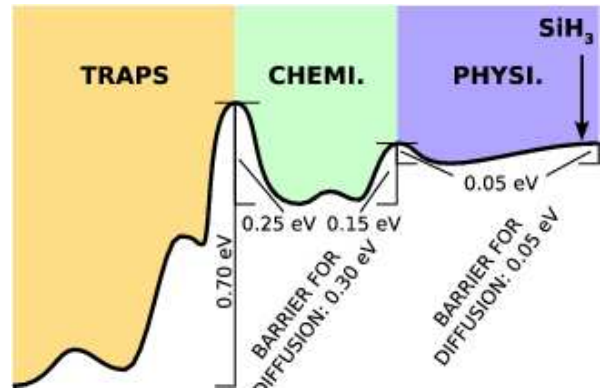
Mechanism	A	B	Mechanism	A	B
a \rightarrow a'	0.30	0.35	c \rightarrow j	0.14	0.27
a \rightarrow b	0.32	0.37	d \rightarrow d'	0.22	0.27
a \rightarrow i	0.17	0.24	d \rightarrow f	0.24	0.39
b \rightarrow b'	0.42	0.55	e \rightarrow f	0.02	0.03
b \rightarrow c	0.26	0.37	g \rightarrow g'	0.22	0.35
b \rightarrow d	0.15	0.28	h \rightarrow j	<0.01	<0.01
b \rightarrow e	0.22	0.37	i \rightarrow i'	0.04	0.03
c \rightarrow g	0.10	0.21	i \rightarrow i''	<0.01	<0.01
c \rightarrow h	0.15	0.27	i \rightarrow j	0.05	0.04

TABLE IV: Energy (eV) of “minima” and “transition states” used in the simplified Kinetic Monte Carlo simulation based on Figure 10. The zero of energy corresponds to the desorb silyl (“silyl” in the table). For simplicity we label as “chemisorbed” (here and in Fig. 10) the bound states of SiH_3 with adsorption energy in the range 0.15-0.35 eV. Prefactors for the “fixed-prefactor” model have been set equal to 1 THz, or twice as large in the presence of two symmetry-equivalent paths. We have also considered rate prefactors ν^* obtained with harmonic transition state theory for selected processes, namely (a) \rightarrow (b) for the reactions starting in a strongly bound state (“chemi” or “trap” in the table), (i) \rightarrow (i') for reactions starting in a physisorbed state, and (i) \rightarrow SiH_3 for desorption. The “forward” and “backward” values for ν^* (THz) used in the simulations of Figure 13 are given.

State	Energy	State	Energy	ν_{\rightarrow}^*	ν_{\leftarrow}^*
trap	-0.59	trap-chemi	0.09	56	28
chemi	-0.15	chemi-physi	-0.01	28	2
physi	-0.05	chemi-chemi	0.15	28	-
silyl	0.00	physi-physi	0.00	2	-
silane	-0.50	physi-silyl	0.00	0.8	-
		physi-silane	0.00	0.8	-

dimer have been investigated in Ref.⁹ within a framework very similar to ours which, however, produced activation energies as high as 0.9 and 0.6 eV for the two process, respectively, as opposed to our values of 0.3 and 0.22 eV. The discrepancy is due to a very different geometry of the transition state which in Ref.⁹ corresponds (both for (a) \rightarrow (a') and (g) \rightarrow (g') jumps) to a silyl nearly flat, sp^2 -like followed by an “umbrella flip” of the hydrogen atoms of the silyl. In our case, by choosing the trajec-

FIG. 10: (color online) Simplified scheme that accounts for most of the features of the complex reactions scheme of Figure 6; the activation energies have to be considered just qualitative estimates, because of both the limited accuracy of DFT calculations and the fact that each of the barriers in this figure corresponds to different pathways with slightly different activation energies (cf. Figure 6). For simplicity we label as “chemisorbed” (here and in Table IV) the bound states of SiH_3 with adsorption energy in the range 0.15-0.35 eV.



tory obtained from the metadynamics simulation as initial MEP in the NEB optimization, we have been able to find a lower transition state involving small deformation of the SiH_3 radical which undergoes a rotation around its C_3 axis during the jump still keeping a sp^3 -like conformation. Indeed, within the NEB method, it is possible that an inappropriate choice of the initial MEP might lead to a reaction path with an activation energy higher than the lowest energy path to the products. Actually, we remark that an even lower barrier (0.17 vs 0.30 eV) for the jump across the channel between two neighboring rows (a) \rightarrow (a') can be obtained along the path (a) \rightarrow (i) \rightarrow (a'), with the physisorbed state (i) as an intermediate. Another issue worth being mentioned is a discrepancy we have found with previous work⁹ on the diffusion mechanism of the silyl along the dimer row. Using LSD-PBE (spin unrestricted calculations) we have not been able to optimize the intermediate state described as a local minimum in Figure 3 of Ref.⁹ (a silyl adsorbed on the five-fold coordinated Si atom of the Si-H group) which has been obtained probably within a spin-restricted (LDA-PBE) framework. In fact, the configuration proposed as a local minimum along the diffusion path in Ref.⁹, transforms in configuration (e), in our NEB optimization. Moreover, by searching for a direct (a) \rightarrow (e) transformation, we have always found configuration (b) as an intermediate minimum. Consequently, we have not been able to find a minimum energy path for a “direct” jump (a) \rightarrow (a'') along the dimer row as reported in Ref.⁹. Probably the discrepancies with previous work might still be ascribed to the neglect of spin polarization in Ref.⁹.

B. Kinetic Monte Carlo

Based on the reaction scheme of Figure 6 we have performed Kinetic Monte Carlo (KMC) simulations of diffusion and desorption of the adsorbed silyl. We have considered a lattice model, each lattice site corresponding to a 2×1 unit cell. At each site different configurations for the silyl, corresponding to the different minima of Table II (and Fig. 6) are possible. We have only omitted configuration (e), as it is only a shallow minimum along the (b) \rightarrow (f) migration pathway, causing frequent oscillation of the system between minima (f) and (e) which slows down dramatically simulations at low (room) temperatures. We have estimated reaction rates ν at different temperatures within transition state theory, i.e. $\nu = \nu^* \exp(-E_a/k_B T)$, with activation energies E_a given in Table III and prefactor ν^* set to 1 THz for all processes. In some cases, for example for the (a) \rightarrow (a') jump, two pathways equivalent by symmetry exists: we have used a 2 THz prefactor in this and similar cases. The choice of a common prefactor is obviously questionable. We have calculated within the harmonic approximation to transition state theory the prefactors for a diffusion process among strongly bound states ((a) \rightarrow (b)), for the diffusion between two physisorbed states ((i) \rightarrow (i')) and for desorption ((i) \rightarrow SiH₃). The prefactor ν^* is given by $\prod \nu_j^{(I)} / \prod \nu_j^{(TS)}$, where $\nu_j^{(I)}$ and $\nu_j^{(TS)}$ are the positive phonon frequencies for the initial and transition states respectively, obtained by diagonalizing the dynamical matrix, calculated in turns by finite displacements of the atoms. For the desorption process, which does not display a saddle point on the potential energy surface along the desorption path, we have instead used the vibrational frequency of the phonon whose displacement pattern is parallel to the minimum energy path. The results, 28 THz ((a) \rightarrow (b)), 2 THz ((i) \rightarrow (i')) and 0.8 THz ((i) \rightarrow SiH₃), differ less than the typical errors in this kind of calculations, which are at least one or two orders of magnitude. Therefore, given the considerable computational resources needed to compute all prefactors, we have judged not worthy to pursue this task at the moment.

Moreover, we have considered a single silyl adsorbed on a perfect H:Si(100)-(2x1) surface which is obviously very far from the real growth conditions in PECVD where partial surface hydrogenation and large coverage of adsorbed species are expected. Still, these simplified KMC simulations can provide crucial information on SiH₃ diffusion to model the behavior of the silyl radical at the more complex conditions of real PECVD growth.

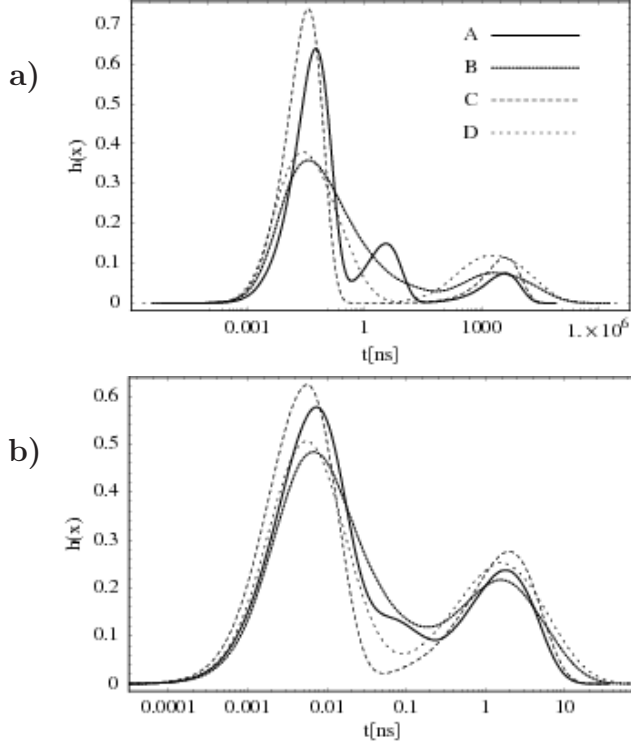
Within our scheme, the final fate of the adsorbed silyl is always desorption, either as a silyl or a silane. The KMC simulations let us estimate the average resident time of the silyl on the surface and the average maximum distance the silyl can travel before desorbing. We have checked the stability of the results versus random variations of the barriers within the typical DFT uncertainties. To this aim, we have performed several sets of

simulations adding a uniform noise with zero mean and ± 0.1 eV width to all the minima and transition states energies in Figure 6, discarding the set of randomized activation energies whenever one of them is negative. Some other sets have also been discarded since they lead the system to oscillate for a long time ($> 10^6$ steps) between two minima separated by tiny barriers. In all simulations the silyl starts from site (a) since it corresponds to the adsorption site observed in dynamical Car-Parrinello simulations of SiH₃ impinging on the surface (cf. Section IIIA).

The calculated distribution of resident times (times before desorption) is reported in Fig. 11, as obtained by averaging over 10^6 KMC simulations. Results with activation energies from Table III and with the energies randomized in every simulation are compared. The distribution of resident times, $h(x)$, is reported as a function of the logarithm of the resident time t ($x = \log_{10} t$), i.e. $\int_{x_1}^{x_2} h(x) dx$ returns the fraction of trajectories with a resident time between 10^{x_1} and 10^{x_2} . In this representation, for an exponential decay ke^{-kt} , the histogram on a logarithmic x -axis has a peak at $-\log_{10} k$. Different peaks on the histogram are therefore related to processes with different desorption rates. The distribution of resident times reveals three peaks at 500 K: a nearly instantaneous desorption from site (a) (low t peak), a desorption from site (g) easily accessible from (a) (peak at intermediate t) and finally desorption from trap states at longer t . The peak due to desorption from site (g) reduces to a shoulder of the first peak in simulations with randomized activation energies. At higher temperatures the probability to reach the traps increases and the importance of longer resident times (area of the peak at the longest t) increases. Therefore, most of the radicals desorb quickly, without reaching the trap states, but a fraction of the adsorbed SiH₃ get to the trap, and remain adsorbed for longer times, of the order of 10^{-5} s at 500 K. The absolute position of the peaks in $h(x)$ depends on the choice of the prefactor ν^* in the reaction rates, but the ratio of different positions and the relative area of the peaks do not.

In Figure 12 we report the results on the average maximum distance the radical can travel before desorbing. For simplicity, only displacement along $[0\bar{1}1]$ are considered. Diffusion distances have been calculated as the displacement along $[0\bar{1}1]$ from the initial site (a); each minimum within the unit cell corresponds to a displacement equal to the relative coordinate of the Si atom with respect to site (a). Averaging over random changes of the barriers results in a variation of the relative importance of diffusion and desorption processes which is significant at room temperature, but negligible at higher temperatures. This is easy to understand, as, at room temperature, the radical would travel very long distances if the barrier for desorption was even a few tens of meV higher than that for diffusion among physisorbed states. Anyway, it is very unlikely that the radical could jump further than few cells before desorbing. The average dif-

FIG. 11: Distribution of resident times t of the silyl on the surface (before desorption). The initial configuration is always the same site (a) (see text). The results are averaged over 10^6 independent KMC runs. The distribution is shown with a logarithmic scale on abscissa ($h(x), x = \log_{10}t$). Panel a) and b) correspond to simulations at $T = 500$ K and $T = 1000$ K, respectively. Curve **A** corresponds to the full reaction scheme, with the energies given in Figure 6. Curve **B** corresponds to the complete scheme, where for each simulation energies for the minima and the transition states have been randomized (see text). Curve **C** and **D** corresponds to the simplified model, with parameters given in Table IV and or with randomized energies (see text), respectively.



fusion lengths in Fig. 12 are independent from the value chosen for the common rate prefactor ν^* .

To investigate the dependence of the diffusion length on the variation of rate prefactors we have considered a simplified model corresponding to Figure 10, with the set of parameters reported in Table IV. Although the model is much simpler than the complete reaction scheme, there are still too many parameters to attempt a significant fitting procedure. We have thus chosen the values in Table IV heuristically, as we only wish to show that the complete scheme is very redundant, and the simplified scheme provides a reasonable description of the behavior of the silyl. In the simplified model only jumps between adjacent cells are considered. Displacement of the silyl among different minima within the same unit cell are not included in the calculation of the maximum average displacement. Firstly, we set all the prefactors equal, as done in the fully detailed KMC, for sake of comparison. The results are reported in Figs. 11 and 12. The sim-

FIG. 12: Maximum distance along $[0\bar{1}1]$ reached by the silyl before desorption as a function of temperature. The results are averaged over 10^6 independent KMC runs. Curve **A** corresponds to the full reaction scheme, with the energies given in Figure 6. Curve **B** corresponds to the complete scheme with randomized activation energies (see text). Curve **C** and **D** corresponds to the simplified model, with parameters given in Table IV and or with randomized energies (see text), respectively. Distances are given in units of the lattice spacing along $[0\bar{1}1]$ ($a_y = 3.84$ Å).

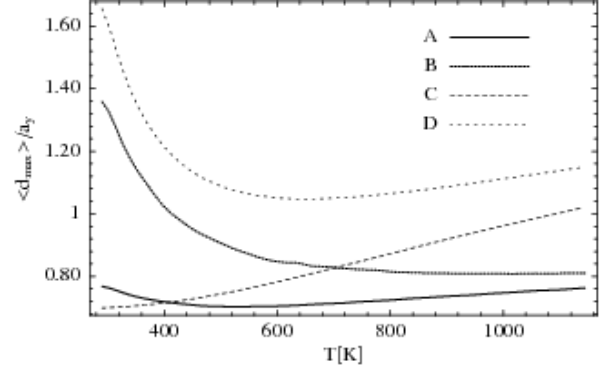
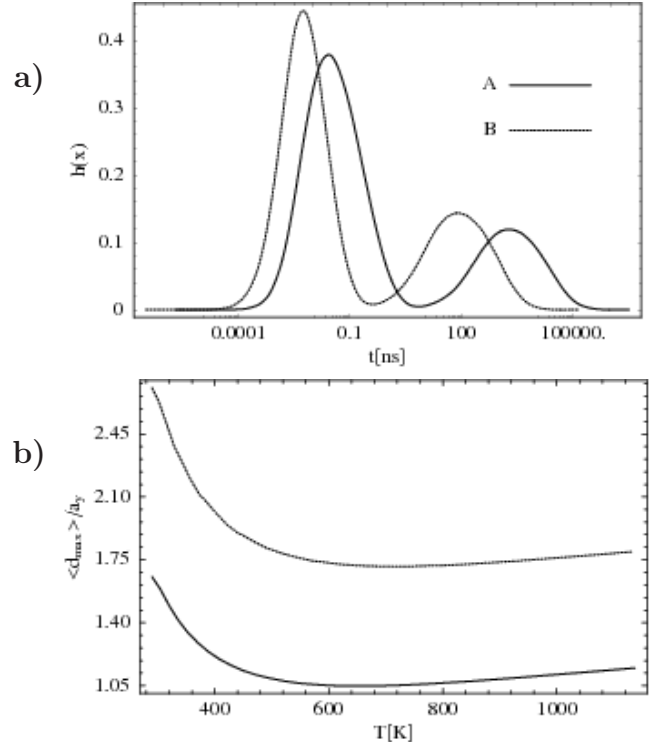


FIG. 13: Comparison of KMC simulations performed on the simplified model and constant prefactors (continuous curve **A**) and with prefactors chosen according to harmonic transition state theory predictions (dotted curve **B**, cf. Table IV). In both cases averages are performed over 10^6 independent KMC runs, with activation barriers randomized as described in the text. a) Distribution of resident times of the silyl on the surface at 500 K (cf. Figure 11). b) Maximum distance along $[0\bar{1}1]$ reached by the silyl before desorption as a function of temperature (cf. Figure 12). Distances are given in units of the lattice spacing along $[0\bar{1}1]$ ($a_y = 3.84$ Å).



plified model is able to reproduce the main features of the complete KMC results. Both the shape of $h(x)$ (but for the smaller structure due to desorption from (g)) and the order of magnitude of the average diffusion length are well reproduced. The simplified model can thus be considered as a good starting point to develop a more elaborate KMC model for realistic conditions with variable H and SiH₃ coverage. Then, we have investigated the dependence of the results on the choice of different prefactors for different reactions. To this aim we have used the prefactors obtained by harmonic transition state theory for the three representative reactions (Table IV). The residence-time histogram (Figure 13) is only slightly shifted. The attempt frequency for diffusion is in this case almost three times the one for desorption, but the average diffusion length is only doubled. This suggests that the model is also relatively stable against changes in the estimated prefactors, making our predictions reliable, despite the unavoidable errors on energies and overall reaction rates. We can therefore conclude that desorption events prevents diffusion of SiH₃ radicals for more than a few lattice spacings. Silyl migration can account for local rearrangement effects, resulting in an increase in the capture area of surface dangling bonds, but cannot be invoked to explain long-range diffusion or surface smoothing on a mesoscopic scale.

IV. CONCLUSIONS

We have investigated the diffusion and desorption mechanisms of the SiH₃ radical adsorbed on H:Si(100)-(2x1) by means of ab-initio calculations. Preliminary metadynamics Car-Parrinello simulations aided us in identifying local minima and diffusion pathways of the the adsorbed silyl. Activation energies and minimum en-

ergy paths for diffusion and desorption have then been refined by NEB calculations. We have identified three classes of adsorption geometries: a set of physisorbed states with low adsorption energy (~ 5 meV), more strongly bound states with adsorption energies in the range 0.15-0.35 eV and a trap state with adsorption energy of 0.6 eV. The silyl can escape from the trap state and diffuse among the other more strongly bound minima. However, by overcoming similar barriers the silyl can move to the physisorbed states from which it can easily desorb. Kinetic Monte Carlo simulations based on the full ab-initio reactions scheme show that the silyl radical can diffuse on average by a few lattice spacing before desorbing in the temperature range 300-1000 K which includes LEPECVD conditions. In contrast with previous works¹⁰, we conclude that diffusion of SiH₃ on H:Si(100)(2x1) surface over length longer than a few lattice spacing is preempted by desorption. Therefore, fast diffusion from H-rich to H-poor regions is not supposed to play a role in promoting the decomposition of SiH₃. Instead, at the experimental conditions of LEPECVD, etching of some surface hydrogen atoms by impinging SiH₃ or H atoms in the plasma is presumably the key factor which promotes decomposition and insertion of SiH₃ adsorbed on a H-rich surface region³⁰.

V. ACKNOWLEDGMENTS

Discussion with C. Cavallotti, S. Cereda, L. Miglio and F. Montalenti are gratefully acknowledged. This work is partially supported by the Cariplo Foundation (SIMBAD project). Computational resources at CINECA has been provided by CNISM through "Iniziativa Calcolo Parallelo 2006".

* Electronic address: michele.cerriotti@phys.chem.ethz.ch; present address: Computational Science, Department of Chemistry and Applied Biosciences, ETH Zürich, USI Campus, Via Giuseppe Buffi 13, CH-6900 Lugano, Switzerland

¹ T. J. Donahue and R. Reif, *J. Appl. Phys.* **57**, 2757 (1985).

² C. Rosenblad, H. R. Deller, M. Döebli, E. Müller, and H. von Känel, *Thin Solid Films* **318**, 11 (1998).

³ C. Rosenblad, T. Graf, J. Stangl, Y. Zhuang, G. Bauer, J. Schulze, and H. von Känel, *Thin Solid Films* **336**, 89 (1998).

⁴ C. Rosenblad, H. R. Deller, T. Graf, E. Müller, and H. von Känel, *J. Cryst. Growth* **188**, 125 (1998).

⁵ M. Kummer, C. Rosenblad, A. Dommann, T. Hackbrth, G. Höck, M. Zeuner, E. Müller, and H. von Känel, *Mater. Sci. Eng.* **B89**, 288 (2002).

⁶ J. R. Abelson, *Appl. Phys.* **A 56**, 493 (1993).

⁷ A. von Keudell and J. R. Abelson, *Phys. Rev.* **B 59**, 5791 (1999).

⁸ F. C. H. Lim, E. S. Tok, and H. C. Kang, *Phys. Rev.* **B**

74, 205333 (2006).

⁹ T. Bakos, M. S. Valipa, and D. Maroudas, *J. Chem. Phys.* **125**, 104702 (2006).

¹⁰ M. S. Valipa, T. Bakos, E. S. Aydil, and D. Maroudas, *Phys. Rev. Lett.* **95**, 216102 (2005).

¹¹ A. Gupta, G. N. Parsons, and H. Yang, *Surf. Sci.* **496**, 307 (2002).

¹² T. Bakos and D. Maroudas, *IEEE Trans. Plasma Sci.* **33**, 230 (2005).

¹³ S. Ramalingam, M. Maroudas, E. S. Aydil, and S. P. Walch, *Surf. Sci. Lett.* **418**, 8 (1998).

¹⁴ S. P. Walch, S. Ramalingam, E. S. Aydil, and D. Maroudas, *Chem. Phys. Lett.* **329**, 394 (2000).

¹⁵ T. Bakos, M. S. Valipa, and D. Maroudas, *J. Chem. Phys.* **122**, 054703 (2005).

¹⁶ T. Bakos, M. Valipa, E. S. Aydil, and D. Maroudas, *Chem. Phys. Lett.* **414**, 61 (2005).

¹⁷ A. Laio and M. Parrinello, *Proc. Natl. Acad. Sci. USA* **29**, 12562 (2002).

¹⁸ M. Iannuzzi, A. Laio, and M. Parrinello, *Phys. Rev. Lett.*

- 90**, 238302 (2003).
- ¹⁹ G. Henkelman and H. Jónsson, *J. Chem. Phys.* **113**, 9978 (2000).
- ²⁰ G. Henkelman, B. P. Uberuaga, and H. Jonsson, *J. Chem. Phys.* **113**, 9901 (2000).
- ²¹ J. P. Perdew, K. Burke, and M. Ernzerhof, *Phys. Rev. Lett.* **77**, 3865 (1996).
- ²² S. Baroni, A. Del Corso, S. de Gironcoli, and P. Giannozzi, <http://www.pwscf.org>.
- ²³ Copyright IBM Corp. 1990-2003, Copyright MPI für Festkörperforschung Stuttgart 1997-2000, <http://www.cpmd.org>.
- ²⁴ R. Car and M. Parrinello, *Phys. Rev. Lett.* **55**, 2471 (1985).
- ²⁵ N. Troullier and J. L. Martins, *Phys. Rev. B* **43**, 1993 (1991).
- ²⁶ D. Vanderbilt, *Phys. Rev. B* **41**, 7892 (1990).
- ²⁷ A. D. Becke, *Phys. Rev. A* **38**, 3098 (1988).
- ²⁸ C. T. Lee, W. T. Yang, and R. G. Parr, *Phys. Rev. B* **37**, 785 (1988).
- ²⁹ J. Härtwig, J. Bak-Misiuk, H. Berger, H. G. Brühl, Y. Okada, S. Grosswig, K. Wokulska, and J. Wolf, *Phys. Stat. Sol. A* **142**, 19 (1994).
- ³⁰ S. Cereda, M. Ceriotti, F. Montalenti, M. Bernasconi, and L. Miglio, *Phys. Rev. B* **75**, 235311 (2007).
- ³¹ S. L. Cunningham, *Phys. Rev. B* **10**, 4988 (1974).
- ³² A. Laio, A. Rodriguez-Forteza, F. L. Gervasio, M. Ceccarelli, and M. Parrinello, *J. Phys. Chem. B* **109**, 6714 (2005).
- ³³ W. G. Hoover, *Phys. Rev. A* **31**, 1695 (1985).
- ³⁴ A. B. Bortz, M. H. Kalos, and J. L. Lebowitz, *J. Comp. Phys.* **17**, 10 (1975).
- ³⁵ A. Matsuda, K. Nomoto, Y. Takeuchi, A. Suzuki, A. Yuuki, and J. Perrin, *Surf. Sci.* **227**, 50 (1990).
- ³⁶ S. Hu, Y. Wang, X. Wang, T. Chu, and X. Liu, *J. Phys. Chem. B* **107**, 2954 (2007).
- ³⁷ K. Tonokura, T. Murasaki, and M. Koshi, *J. Phys. Chem. B* **106**, 555 (2002).